Liu et al. *Microsystems & Nanoengineering* (2026)12:21
https://doi.org/10.1038/s41378-025-01132-w

Microsystems & Nanoengineering
www.nature.com/micronano

ARTICLE Open Access

Functional 2D MoS_2 NEMS resonator array with independent electronic tunability based on mass transfer printing

Zuheng Liu[1], Lingyu Zhu[1], Shuai Yuan[1], Yijian Zhang[1], Pengcheng Zhang[1], Zhenggang Cai[2], Liwei Liu[2]✉ and Rui Yang[1,3]✉

Abstract

Resonant nanoelectromechanical systems (NEMS) based on two-dimensional (2D) materials exhibit excellent resonance properties such as a large tuning range, ultralow power, and large dynamic range, leading to broad potential applications in sensing and signal processing. However, scalable fabrication of high-performance 2D NEMS arrays, particularly those with individually addressable electronic control, remains challenging and underexplored. Here, we report a mass transfer printing (MTP) method for the fabrication of large-scale electronically-independent molybdenum disulfide (MoS_2) NEMS resonators with regular isolation spacing. MoS_2 is precisely torn at the edges of polymer protrusions by the surface tension of auxiliary liquid, followed by dry-transfer to the pre-patterned substrate with microtrenches and electrodes. The MTP technique avoids lithographic processes that could lead to collapsing or failure of suspended 2D materials while obtaining electronically independent devices. Characterization of 84 monolayer MoS_2 NEMS resonators demonstrates maintained material quality after transfer, structural integrity, highly tunable resonance frequencies in very-high-frequency (VHF) band, consistent tuning trend of quality (*Q*) factors, and significant signal-to-noise ratios (*SNRs*). Independent AC voltage excitation and DC voltage sweeping on different resonators confirm individual electronic control without crosstalk even for neighboring resonators. Furthermore, we design and experimentally demonstrate a functional decimal-to-binary converter building block using adjacent, electrically isolated resonators on a single chip, using gate voltage as input and amplitude at the specific frequency as output. The MTP-fabricated array of independently-addressable MoS_2 resonators advances the large-scale integration of 2D NEMS devices, offering a straightforward and promising pathway for a plethora of applications built upon such device platform.

Introduction

Nanoelectromechanical systems (NEMS) based on two-dimensional (2D) materials, such as graphene and transition metal dichalcogenides (TMDCs), exhibit excellent properties such as the resonance frequency above 1 GHz, broad electronic frequency tuning range exceeding 1300%, dynamic range up to 110 dB, broad tuning of quality (*Q*) factor above 400%, rich nonlinear dynamics, and coupling in various physical domains, which benefit from the fantastic mechanical and electronic properties of 2D materials[1–9]. These device properties make 2D NEMS resonators highly promising for numerous potential applications, including high-precision sensing, radio-frequency signal processing, ultralow-power mechanical memory/computing, and compact quantum devices[10–19]. Towards these applications, a reliable mass fabrication technique is critical for the scalable integration of 2D NEMS resonators on chip. Furthermore, by improving the preparation process and applying further treatments such as thermal annealing or strain engineering, there is still significant room for improving the performance of these

Correspondence: Liwei Liu (liweiliu@fudan.edu.cn) or Rui Yang (rui.yang@sjtu.edu.cn)
[1]Global College, Shanghai Jiao Tong University, Shanghai, China
[2]Frontier Institute of Chip and System, Fudan University, Shanghai, China
Full list of author information is available at the end of the article
These authors contributed equally: Zuheng Liu, Lingyu Zhu

devices, which can further expand the application prospects of 2D NEMS resonators[20–23].

The fabrication of 2D NEMS resonator arrays based on various techniques has been reported. The 2D material and contact electrodes can be lithographically patterned on the substrate, followed by a wet chemical etching process of the sacrificial layer underneath, resulting in suspended 2D structures[24]. Yet the atomically-thin layered structure, ultrasmall mass, and high surface-to-volume ratio, which provide the desirable properties for 2D NEMS resonators, also pose challenges for the fabrication of these suspended atomic membranes; especially, the exposure to wet chemicals such as hydrofluoric acid can affect the material properties and stress uniformity, and even lead to device failure or collapse. To avoid contact with wet chemicals, a fully dry transfer technique has also been developed, which relies on a polymer stamp to transfer the whole 2D thin film onto the pre-fabricated surface microtrenches on the substrate, and thus can reduce the chemical residue on the material and the chance of device failure[25–29]. For large-scale array fabrication, 2D materials grown by chemical vapor deposition (CVD) or metal-organic CVD (MOCVD), rather than thin flakes prepared by mechanical exfoliation from bulk material, are commonly used, resulting in continuous 2D material films. Due to the requirement of independent electronic access and electrostatic tuning of different devices in potential applications, a continuous 2D conductive film is not suitable and requires further patterning. However, after suspension of the atomically-thin membranes, lithographic processes can hardly be employed for patterning the membranes due to the high chance of material failure. Therefore, it is necessary to develop a fabrication process for independently-accessible 2D resonator arrays with high reliability.

In this work, we demonstrate the fabrication of independently-accessible monolayer and few-layer MoS_2 NEMS resonator arrays, where devices are physically separated based on a mass transfer printing (MTP) technology. Instead of a flat polydimethylsiloxane (PDMS) layer, we use a custom PDMS polymer stamp with micrometer-scale protrusions as the assist layer for dry transfer of CVD MoS_2 film, which allows the liquid-tension-induced cut of material on the edges, and pick-up of 2D MoS_2 only in the areas with the protrusion. Then, after the dry transfer of the 2D material onto the substrate with microtrenches with precise alignment, we characterize the suspended 2D flakes, demonstrating their suspension over the microtrenches with desirable material properties. We then perform optical interferometry measurement of nanomechanical resonances using either electronic or photothermal excitation on 63 monolayer MoS_2 NEMS resonators with a diameter of $d = 2$ μm within a random region in the array, demonstrating the measured resonance frequencies, Q factors, signal-to-noise ratios (*SNR*s), and the consistency of gate tuning properties. To demonstrate the adaptability of such MTP technique, we further fabricate and measure 15 monolayer MoS_2 NEMS resonators with $d = 3.5$ μm, and 6 few-layer MoS_2 NEMS resonators. We demonstrate independent control of two groups of physically-separated 2D devices by applying different AC voltage signals or DC voltage sweeps to the electrodes connected to each group, respectively, and show no crosstalk between the electrically isolated devices. Furthermore, leveraging the independent electrical accessibility, we design and demonstrate a functional decimal-to-binary converter building block based on two adjacent and separated resonators on a single chip, demonstrating the functional characteristics of the device array. The results show high promise for building large-scale functional arrays based on 2D NEMS resonators, towards sensing, signal processing, and analog-based computing.

Results and discussion

MTP technology for 2D NEMS fabrication

The fabrication of the physically-isolated 2D NEMS MoS_2 resonator arrays follows an MTP-based process[30,31]. Firstly, a substrate with a periodic array of microtrenches and metal electrodes is fabricated using standard photolithography, microtrench etching *via* reactive ion etching (RIE), and 10 nm chromium (Cr) / 40 nm gold (Au) metal electrodes deposition *via* electron beam evaporation (Supplementary Note S1). Additionally, we prepare the soft PDMS stamp with matched array designs of square micro-protrusions (20 × 20 × 10 μm in length, width, and height, respectively) with 20 μm spacing, as the transfer-assist polymer layer, *via* a SU-8 photoresist based soft lithography and PDMS replica molding (Fig. 1i and Supplementary Note S2). After the CVD growth of monolayer and few-layer MoS_2 on oxidized Si substrate, we bring the protrusions on the PDMS polymer and the 2D material flake into close contact and apply appropriate pressure, leaving the bare MoS_2 in the non-contact regions (intervals) (Fig. 1a, b).

Then, a 1:1 isopropanol (IPA)/ deionized (DI) water solution is prepared and dropped along the contact edge between polymer and 2D material, which facilitates the wetting (Fig. 1b)[32], and makes the liquid penetrate the interface between MoS_2 and SiO_2, separating the material from the substrate *via* capillary force[33,34]. In the contact regions, MoS_2 adheres to the PDMS protrusions due to van der Waals (vdW) forces, while the non-contact regions will be curled or torn from the edge due to the relatively strong liquid surface tension (Fig. 1c). Due to the hydrophobic nature of the dense micro-patterns on the stamp, the use of an isopropanol aqueous solution, compared to pure water, results in a lower surface tension

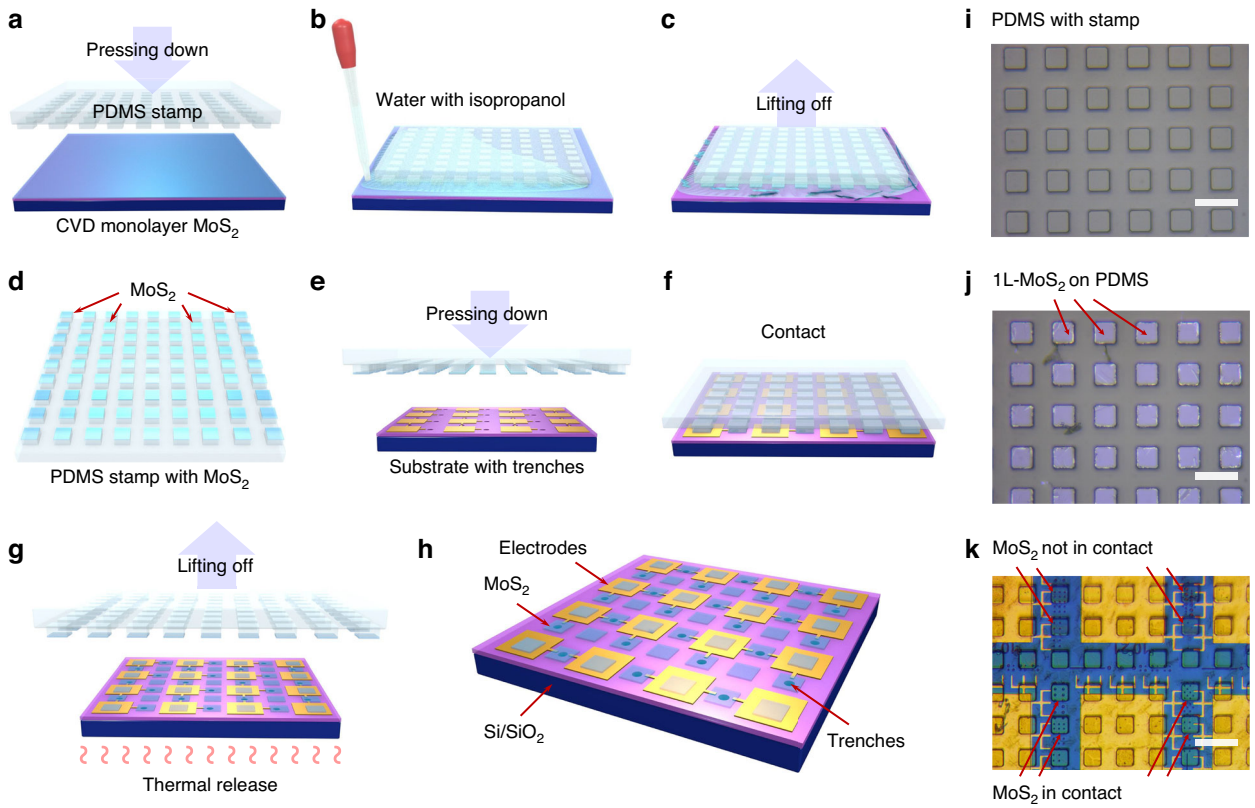

Fig. 1 Fabrication process of the independent accessible resonators using MTP technology with a PDMS stamp. a The transfer of CVD-grown MoS_2 onto the PDMS polymer stamp, starting with the contact between MoS_2 and protrusions, and the bare PDMS stamp optical image is shown in (i). *Scale bar*: 40 μm. **b** A 1:1 IPA / DI water solution is dropped along the contact edge between polymer and growth substrate, which penetrates rapidly into MoS_2-substrate gap *via* capillary action. **c** After separation driven by capillary forces, the MoS_2 attached to the stamp is stripped from the substrate. **d** Schematic of the PDMS stamp with the attached MoS_2. The corresponding optical image of PDMS with monolayer (1 L) MoS_2 is shown in (**j**). *Scale bar*: 40 μm. **e**, **f** Alignment of the MoS_2 on PDMS protrusions with substrate patterns and smooth contact establishment, with (**k**) showing an optical image during MTP process. *Scale bar*: 50 μm. **g** Lift-off of PDMS stamp after thermal release of the MoS_2 film, leaving the 2D material on the substrate to form NEMS resonators over pre-designed microtrenches. **h** Schematic of the independently-accessible resonator array. Square MoS_2 structures (20 μm edge length) with 20 μm spacing are transferred onto the substrate, with each MoS_2 square electronically isolated, and controlled *via* connected electrodes without mutual interference. **i**–**k** Optical images of the PDMS and substrate during MTP

of the liquid, thereby facilitating a smooth wetting process. Meanwhile, the capillary effect enables the auxiliary liquid to be rapidly drawn into the gap between the liquid and the substrate, thereby accelerating the infiltration process. In contrast, if only pure isopropanol is used, its surface tension is too low to tear and cut the MoS_2 at the edges of the PDMS stamp protrusions. After complete liquid infiltration and material separation, the growth substrate is gently separated from the assist layer, yielding a transfer stamp with an intact, almost crack-free monolayer MoS_2 after drying in ambient environment (Fig. 1d, j, with detailed optical images in Fig. S4).

Next, we print the monolayer MoS_2 onto the target substrate using a custom-built transfer stage consisting of four movable axes (X,Y,Z, and a rotation R axis in the XY plane), following steps similar to a dry transfer process[33]. Because PDMS volume is highly temperature-dependent, the initial transfer temperature before contact should be maintained at room temperature to improve efficiency and minimize misalignment[35]. With the PDMS stamp close to the target substrate, we carefully adjust the relative angle between the stamp and the target substrate by rotating the R-axis, so that the protrusions of the stamp are parallel to the edges of the electrode. Then, we move the substrate in the XY axes to ensure that the MoS_2 patterns on the PDMS protrusions precisely cover the microtrenches and contact the electrodes, and finally adjust the Z axis to bring the MoS_2 into contact with the substrate. Before contact, we maintain a constant temperature to prevent 2D material from breaking (Fig. 1e, f, k). By comparison with PDMS with higher protrusions (20 μm), we further observe that PDMS protrusions with lower height (10 μm) deform and twist less under the contact pressure, aiding in maintaining flatness and integrity of the MoS_2 (Supplementary Note S4). Next, we slowly and

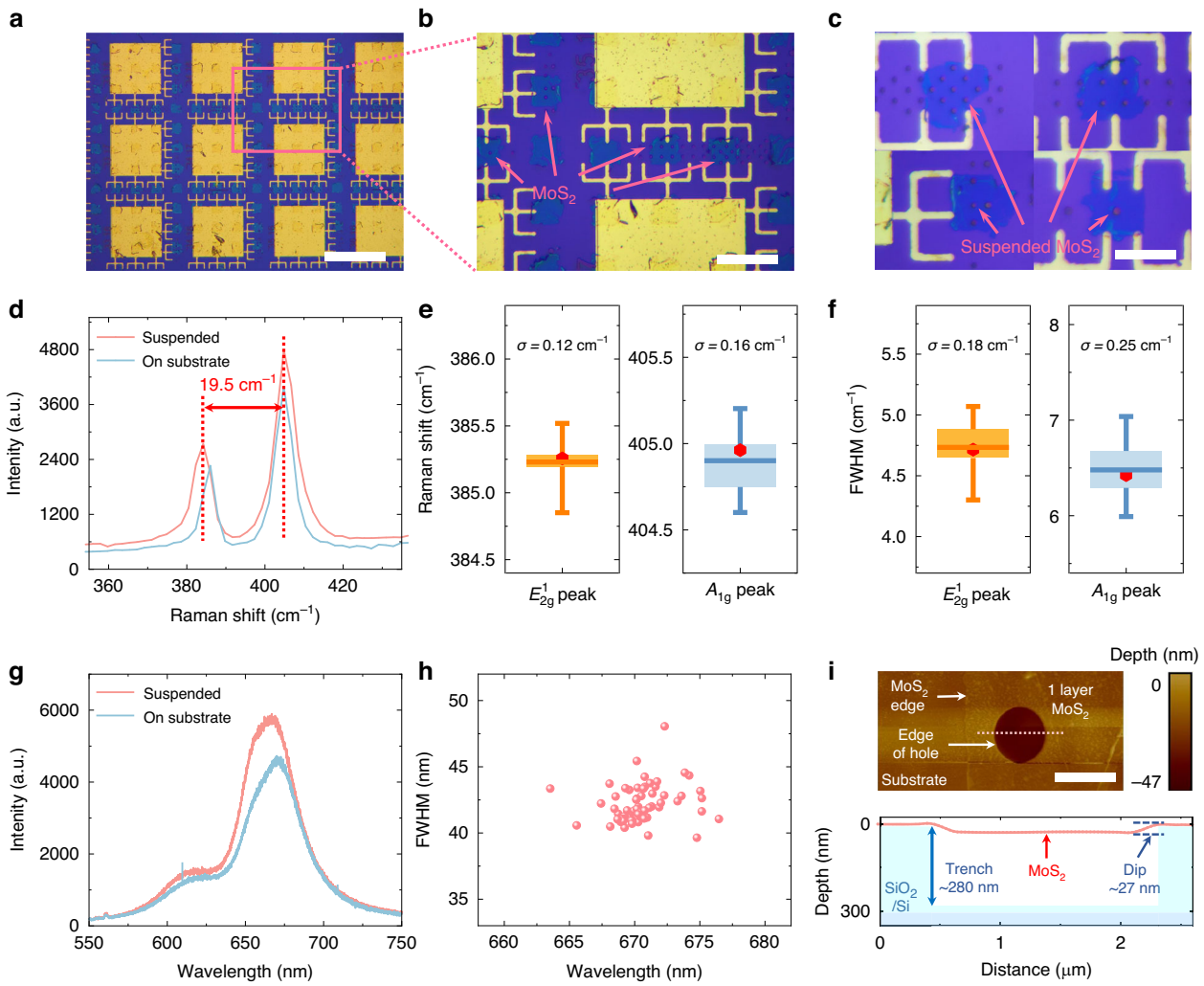

Fig. 2 Characterization of the suspended monolayer MoS_2 NEMS resonator array fabricated by the MTP process. Optical images at magnifications of (**a**) 20×, (**b**) 50×, and (**c**) 100×, with scale bars of 100 μm, 40 μm, and 20 μm, respectively. **d** Representative Raman spectra from suspended regions over microtrenches (red) and substrate-supported regions (blue) of the transferred monolayer MoS_2. Statistics of the (**e**) Raman peak positions, and (**f**) FWHM values for the A_{1g} (blue) and $E_{2g}{}^1$ (orange) modes for 63 devices, with the long bar and red hexagon representing the average and median, respectively. **g** Representative photoluminescence (PL) spectrum from suspended regions over trenches (red) and substrate-supported regions (blue) of MoS_2. **h** Summary of FWHM values for the dominant PL peak across the 63 devices. **i** AFM topology measurement of a suspended MoS_2 membrane over the microtrench, with the substrate, material edge, device edge, and membrane dip in the suspended region labeled. *Scale bar*: 2 μm

gently heat the substrate in contact with 2D material and PDMS to ~70 °C, thermally releasing the MoS_2 from the PDMS and adhering it to the target substrate *via* vdW forces. The polymer layer is then gently lifted, leaving the MoS_2 on the substrate, and forming suspended MoS_2 over the microtrenches (Fig. 1g). Such a process naturally divides the MoS_2 into arrays of isolated 20-micron squares, which avoids electronic interference and enables independent control of each device in the array (Fig. 1h).

Characterization of material properties

Optical images at varying magnifications show the intact transfer of 2D MoS_2 NEMS resonator arrays with 20 × 20 μm lateral dimensions and 20 μm pitch, which confirms that the MTP process is an efficient technology for the scalable fabrication of 2D NEMS resonator arrays (Fig. 2a–c). Uniquely designed interdigitated electrodes are patterned and connected to the square MoS_2 arrays to enhance device density while ensuring the mechanical integrity of the MoS_2. We then employ Raman spectroscopy to assess the quality of the transferred MoS_2 array. Raman spectra show monolayer MoS_2 material from the peak separation (Fig. 2d)[36,37], with a red shift in the suspended region over the trench indicating strain[38]. Statistical analysis of the $E_{2g}{}^1$ and A_{1g} Raman modes across 63 devices with the same diameters validates the high

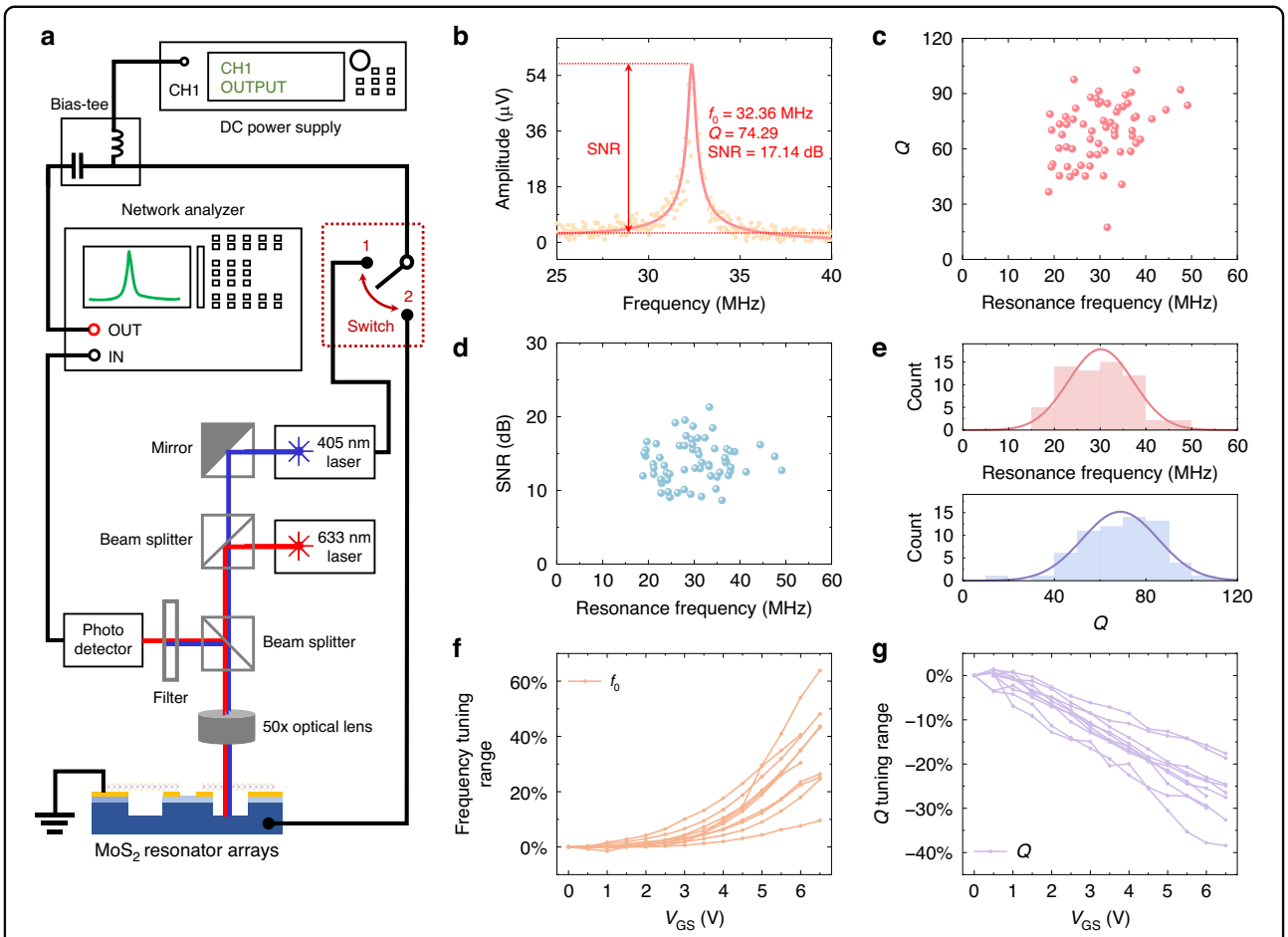

Fig. 3 Measured resonant properties of monolayer MoS_2 NEMS resonator arrays by MTP technology *via* photothermal excitation and capacitive excitation. a Optical interferometry measurement setup using a 633 nm He-Ne laser. Resonance is driven either photothermally (Port 1, fixed 0.5 V DC + 0.5 V AC is adopted if selected) or capacitively by DC plus AC voltages (Port 2). **b** Resonance properties including the resonance frequency, *Q* factor, and *SNR* for a device, showing measured data (orange symbols) and fitting curve (red line). Statistical analysis of (**c**) resonance frequency *vs.* *Q* factor, and (**d**) frequency *vs.* *SNR*, for 63 devices. **e** Distributions of resonance frequency and *Q* factor, with fitting curves using normal distribution. Electronic tuning of (**f**) resonance frequency and (**g**) *Q* factor under capacitive excitation for 10 representative resonators, as V_{GS} increases with a fixed $v_{ac} = 30$ mV, showing that the resonance frequency increases with V_{GS} from 0 V to 6.5 V, and *Q* factor decreases with V_{GS}, with consistent trends across devices

uniformity of the monolayer MoS_2 material after transfer using the MTP technique, with the peak positions and full-width-at-half-maximum (FWHM) values showing minimal variations, which can be indicated by their narrow distributions and small standard deviation σ (Fig. 2e, f, and Fig. S19). The high lattice quality from Raman measurements also confirms that the MTP technique introduces minimal damage to MoS_2, consistent with previous reports[30,39].

We also measure the photoluminescence (PL) spectra from the 63 devices to further confirm the thickness and lattice quality. A single peak at ~670 nm with high intensity confirms the monolayer nature of the MoS_2 (Fig. 2g)[40]. The narrow and uniform FWHM values of the dominant PL peak (39.6 to 48.0 nm) underscore the material homogeneity and transfer reproducibility (Fig. 2h)[41]. Beyond the intrinsic lattice quality and layer number, it is essential to confirm device continuity over trenches after transfer. Atomic force microscopy (AFM) topography provides direct evidence for successful device suspension with complete, conformal coverage over the microtrench structures (Fig. 2i). The line profile across the ~280 nm high microtrench confirms the continuity of the suspended MoS_2 membrane with ~27 nm deformation, presumably caused by the downward pressure during transfer.

Resonance properties of the 2D MoS2 resonator arrays

We characterize the resonances of the arrays using a custom-built optical interferometry system (633 nm He-Ne laser), with the chip placed in a vacuum chamber at room temperature, and excited capacitively or with photothermal actuation (Fig. 3a)[42–44]. In this system, a DC voltage from a

source and a sweeping AC voltage from a network analyzer are connected to a bias-tee, then routed to either the 405 nm amplitude-modulated blue laser (Port 1, a fixed 0.5 V DC ± 0.5 V AC voltage combination is adopted if selected) or the global gate electrode (Port 2, DC and AC with variable magnitude and frequency is adopted if selected). From the measured resonance spectra from photothermal excitation, we extract the resonance frequency, Q factors, as well as the *SNR*s *via* peak analysis (Fig. 3b). We have measured and analyzed 63 devices with 2 μm diameter, and summarized the frequencies *vs.* Q factors, and frequencies *vs. SNR*s as scatter plots (Fig. 3c, d; detail in Supplementary Note S5). Additionally, resonance frequencies and Q factor distributions for all resonators conform to normal distribution, centered at ~30 MHz and 70, respectively (Fig. 3e). These results demonstrate that the array exhibits consistent characteristics, with all devices showing resonance in the VHF band.

To further explore the tuning performance of the resonators, we apply DC (V_{GS}) and AC (v_{ac}) voltages between the back gate and drumhead of each device (port. 2), driving resonance and sweeping V_{GS} to tune frequency and Q factor *via* static deflection and strain modulation. Resonance frequencies and Q factors are extracted for each resonance as V_{GS} is swept from 0 to 6.5 V in 0.5 V steps at a fixed $v_{ac} = 30$ mV, for 10 representative devices. The frequency tuning range is calculated as the difference of resonance frequencies and the initial resonance frequency measured at $V_{GS} = 0$ V, divided by the initial resonance frequency: $(f_{res}\text{-}f_0)/f_0$, showing a consistent increase due to the large tensile strain with increasing V_{GS} (Fig. 3f), described by:

$$f = \frac{1}{2\pi}\sqrt{\frac{2.405^4 E_Y \varepsilon_r}{2\rho R^2} - \frac{\epsilon_0}{0.75\rho t g^3}V_{GS}^2}$$

where t, E_Y, ν, and ρ are the thickness, Young's modulus, Poisson's ratio, and mass density, respectively, R is the radius, ε_r is the gate-tunable total strain, g is the initial gap depth, ϵ_0 is the vacuum permittivity[45]. Similarly, we also obtain the Q factor tuning range by taking the difference between the Q factors and the initial Q factor at $V_{GS} = 0$ V, divided by the initial Q factor: $(Q\text{-}Q_0)/Q_0$, showing a decrease with V_{GS} for these fully-clamped resonators (Fig. 3g), attributed to the combined effects of increased tensile strain and vibration amplitude, which is in accordance with previous Q tuning model[46]:

$$Q_{TED}^{-1} = \frac{5.576x_0^2}{\varepsilon_r(V_{GS})R^2(1-\nu^2)}\delta$$

where δ is a fitting parameter (related to the material and device structure), ε_r (V_{GS}) is gate-tunable strain, x_0 is the resonance amplitude proportional to $|V_{GS}\times v_{ac}|$ under linear damping. Since $Q_{Total}^{-1} = Q_{TED}^{-1} + Q_{Others}^{-1}$, ($Q_{Others}^{-1}$ is independent of V_{GS}), an increasing Q_{TED}^{-1} reduces the total Q. The arrays exhibit consistent electronic tuning of resonance frequencies and Q factors with V_{GS}.

In order to verify that MTP technology is also applicable to the fabrication of 2D NEMS resonators of various sizes and thicknesses, we further employ MTP to fabricate 15 monolayer MoS_2 NEMS resonators with different sizes and 6 few-layer MoS_2 NEMS resonators, demonstrating the MTP method's applicability across different sizes and thicknesses. For monolayer MoS_2 NEMS resonators with diameters of 3.5 μm, the resonances also show relatively uniform properties, with lower resonance frequencies compared with resonators with $d = 2$ μm (Figs. S13–S14). The few-layer devices generally show relatively worse material integrity compared with monolayer counterparts, likely due to the difficulty of fracturing the few-layer materials from the edges (Supplementary Note S6, Fig. S9–S12). We also measure clear resonances for these few-layer MoS_2 NEMS resonators (Fig. S15).

Independent electronic control of 2D NEMS resonator arrays

Leveraging the MTP technology, we demonstrate device-level individual modulation capabilities because the MTP process achieves pre-segmentation prior to transfer onto the substrate, distinct from previous continuous-membrane 2D NEMS resonator arrays[25,47]. We validate independent control by applying distinct AC excitation voltages (v_{ac}) and DC voltage sweeps (V_{GS}) on four resonators in two adjacent electrode groups and characterize their responses. As illustrated in Fig. 4a, Device 1 and Device 2 share the electrode A, while Device 3 and Device 4 share the electrode B. With a global fixed V_{GS} of 3 V to induce electrostatic force, a 30 mV v_{ac} excitation is applied to electrode A with electrode B grounded. Therefore, we measure clear resonances from Devices 1 and 2 (electrode A), while Devices 3 and 4 (electrode B) show no response (Fig. 4b, c). This confirms that AC excitation on electrode A does not affect devices connected to electrode B, confirming the electronic isolation between resonators. To further assess the potential crosstalk, we repeat the measurements using the same resonators by exciting the neighboring device with the non-excited devices floating. The spectral response indicates that the floating device remains idle (Supplementary Note S11), further confirming that the crosstalk among devices is negligible. Conversely, with the same global DC gate bias (3 V), v_{ac} of 30 mV is applied to electrode B with electrode A grounded (Fig. 4d), so Devices 1 and 2 remain inactive, whereas Devices 3 and 4 are excited with resonances measured (Figs. 4e, f). Some difference in the *SNR* of the resonances could be related to the vibration

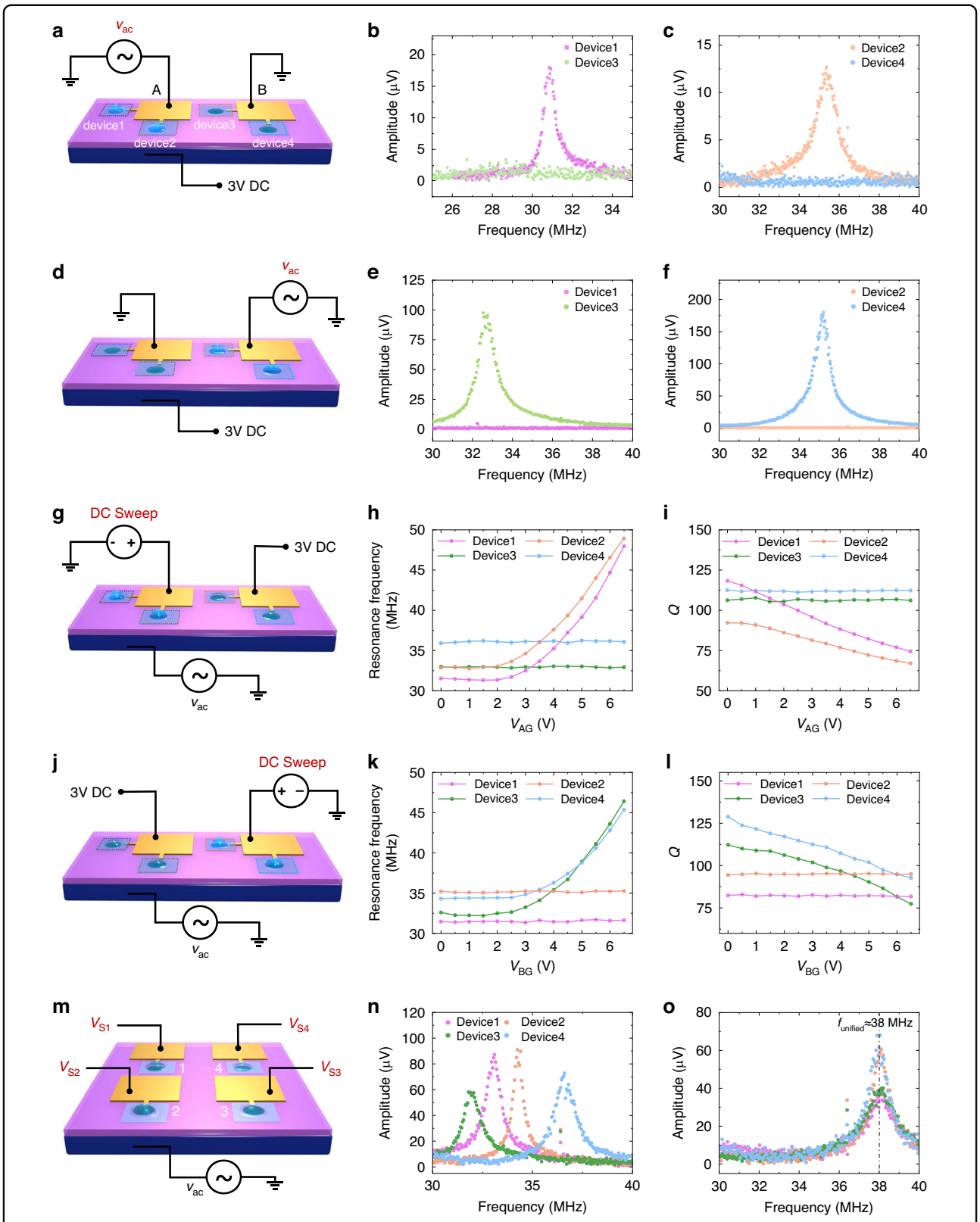

Fig. 4 (See legend on next page.)

(see figure on previous page)
Fig. 4 Electronically-isolated operation in MTP-fabricated 2D NEMS resonator arrays. a Schematic illustration of the device configuration: global $V_{GS} = 3$ V, and $v_{ac} = 30$ mV on electrode A. Devices 1-2 are controlled by electrode A; Devices 3-4 are grounded *via* electrode B. Resonance spectra measured under electrode-A excitation: (**b**) Device 1 is activated and Device 3 is idle; (**c**) Device 2 is activated and Device 4 is idle. **d**–**f** Measurements with a global $V_{GS} = 3$ V, and $v_{ac} = 30$ mV on electrode B, shown in the same sequence as in (**a**–**c**). **g** Schematic illustration of the device configuration: a global $v_{ac} = 30$ mV, DC voltage V_{AG} sweeps from 0 to 6.5 V on electrode A (V_{AG}), and a fixed $V_{BG} = 3$ V is applied on electrode B. Strain-induced (**h**) resonance frequency and (**i**) Q tuning in Devices 1-2 with V_{AG} sweep, with Devices 3-4 (electrode B) maintaining constant resonance frequency and Q. **j**–**l** Measurements with a global $v_{ac} = 30$ mV, DC voltage V_{BG} sweeping from 0 to 6.5 V on electrode B, and a fixed $V_{AG} = 3$ V on electrode A, shown in the same sequence as in (**g**–**i**). Demonstration of resonance frequency compensation by V_{GS} for four adjacent devices, showing (**m**) illustration of device connection, (**n**) the initial resonances when V_{S1} to V_{S4} are the same for four isolated devices, and (**o**) the resonances with voltage compensation, with additional 1.7 V, 1.9 V, 1.95 V, and 1.4 V voltages applied at V_{S1} to V_{S4}, respectively

amplitude of the device itself, optical responsivity of the laser interferometry measurement, Q factor, position of the laser spot, and the noise level[48].

Beyond AC excitation, we further investigate the independent electronic frequency tuning, and prove that there is negligible crosstalk between isolated devices during the DC sweep. With a global v_{ac} of 30 mV and a DC sweep (0–6.5 V) on electrode A to modulate the tensile strain in Devices 1 and 2, electrode B receives a fixed 3 V bias (Fig. 4g). For Devices 1 and 2, a consistent increase of resonant frequency with increasing DC voltage due to enhanced tensile strain is observed, while Devices 3 and 4 maintain nearly fixed resonant frequencies. Correspondingly, Fig. 4i shows the strain-modulated Q factor for Devices 1 and 2 connected to electrode A, while Devices 3 and 4 connected to electrode B are unaffected. In contrast, with a global v_{ac} of 30 mV, a fixed 3 V bias on electrode A, and a DC sweep (0–6.5 V) applied to electrode B (Fig. 4j), Devices 3 and 4 exhibit resonant frequency and Q factor tuning, while Devices 1 and 2 maintain stable frequency and Q (Fig. 4k, l). These results demonstrate independent electronic control of devices within the MTP-fabricated large-scale 2D NEMS resonator arrays, immune to interference from adjacent electrodes.

In the frequency response of the array, while the resonators have relatively consistent properties, some variations in resonance responses due to the material or the fabrication process could still exist (Fig. 4m, n). Fortunately, gate voltage can easily tune the resonance frequency, and the resonators are electronically isolated, which allows us to compensate for the variations in resonance frequency and unify the frequencies, by applying appropriate and different gate voltages to different devices. We measure four adjacent yet electronically independent devices to verify such a voltage compensation technique (Fig. 4o). To unify the resonance frequencies, we apply additional compensation voltages of 1.7 V, 1.9 V, 1.95 V, and 1.4 V to V_{S1} through V_{S4}, respectively, and observe that the resonance frequencies of all four devices increase and are unified at approximately 38 MHz. Such a voltage compensation technique enabled by independent electronic tuning shows the advantage of MTP technology for functional 2D NEMS applications.

Functional decimal-to-binary converter building block based on independent 2D NEMS resonator arrays

By leveraging the independent excitation and tuning of 2D NEMS resonators, we design a two-bit decimal-to-binary converter building block using two adjacent yet independent devices, and demonstrate its basic logic function. The DC gate voltage serves as the input, while the vibration amplitudes of the two devices constitute a two-bit binary output. As the foundation for implementing the conversion functions, resonators A and B receive constant DC voltages of 1.5 V and 3 V at their source electrodes, respectively (Col. 4-5 in Fig. 5b). Additionally, a fixed 30 mV AC voltage is applied to the global gate *via* a bias-tee to excite the vibrations, with the vibration amplitude converted to voltage by the laser interferometer and photodetector (Fig. 5a). In a two-bit conversion scheme, decimal inputs '0', '1', '2', and '3' correspond to binary outputs '00', '01', '10', and '11', respectively (Col. 1-3 in Fig. 5b). The silicon substrate functions as the global gate, to which DC voltages of −2 V, −1 V, 6 V, and 7 V are applied to represent decimal inputs '0', '1', '2', and '3', respectively (Col. 6 in Fig. 5b). Switching the input changes the V_{GS} for both devices, thereby modifying their resonant frequencies through strain variation.

During operation, a fixed working frequency is selected such that the shifts in the resonant frequency result in measurable changes in vibration amplitude. An amplitude threshold V_{TH} of 6 μV is defined to digitize the output: signals above this threshold are interpreted as logic '1', and those below as logic '0'. By applying input voltages corresponding to '0' through '3', we measure the resonance spectra of both devices (Fig. 5c, d). For input '0', '1', '2', and '3', the actual voltages applied between the gate and source of device A (V_{GSA}) are 3.5 V, 2.5 V, 4.5 V, and 5.5 V, respectively (Col. 7 in Fig. 5b). Conversely, the voltages applied between the gate and source of device B (V_{GSB}) are 5 V, 4 V, 3 V, and 4 V, respectively (Col. 8 in Fig. 5b). This flexibility in V_{GS} adjustment compensates for device-to-device variability due to material or fabrication non-uniformity, and sets up the resonator frequencies to the desirable values.

To fulfill the conversion requirements, Device A (bit 1) should output '0' (amplitude < V_{TH}) for inputs '0' and '1',

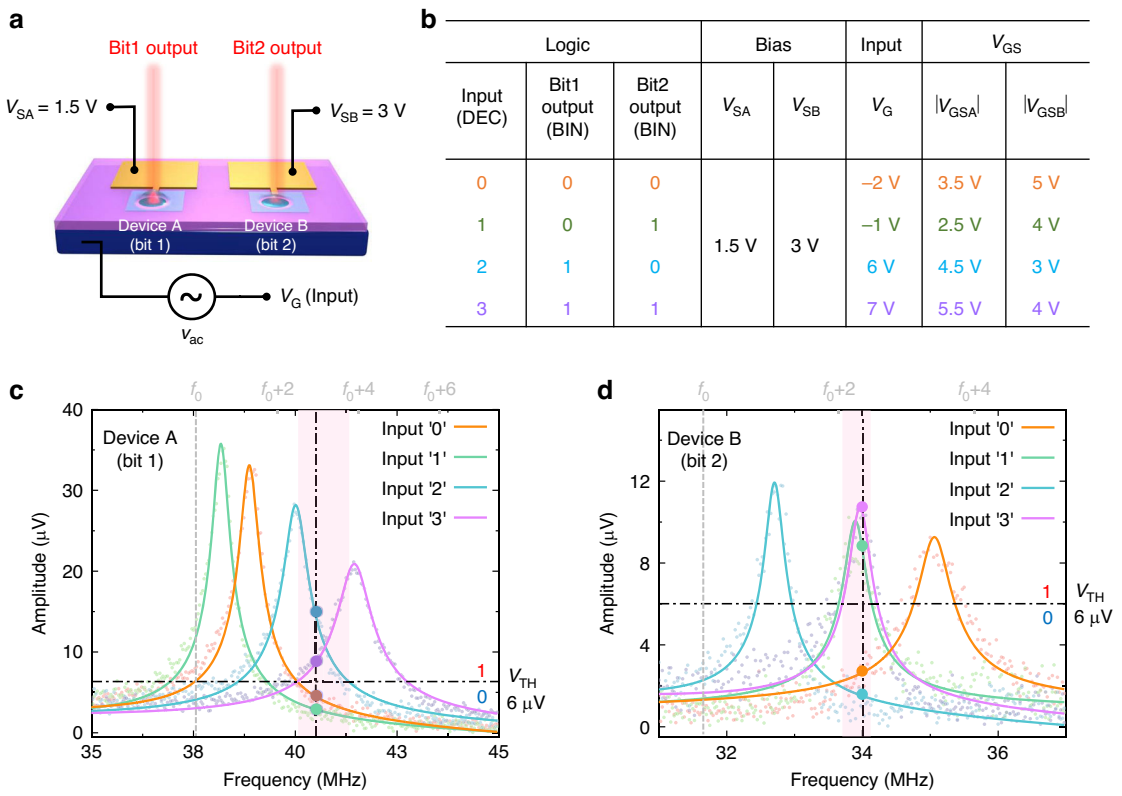

Logic			Bias		Input	V_{GS}	
Input (DEC)	Bit1 output (BIN)	Bit2 output (BIN)	V_{SA}	V_{SB}	V_G	$\|V_{GSA}\|$	$\|V_{GSB}\|$
0	0	0	1.5 V	3 V	–2 V	3.5 V	5 V
1	0	1			–1 V	2.5 V	4 V
2	1	0			6 V	4.5 V	3 V
3	1	1			7 V	5.5 V	4 V

Fig. 5 Design and verification of a decimal-to-binary converter building block based on two adjacent devices in the electronically-independent 2D resonator array. a Schematic of the 2D NEMS decimal-to-binary converter building block. The global gate voltage serves as the input, while the vibration amplitudes of the two resonators at specifically chosen operating frequencies are used as the output. A constant 30 mV AC voltage is applied to the global gate to drive vibrations. Different DC gate biases (1.5 V for A, and 3 V for B) are applied to the sources to enable logic functionality. **b** Truth table of the converter building block, the constant bias, input gate voltages, and the corresponding V_{GS} values for both devices. **c** Measured output of Device A (Bit 1): Output '0' for inputs '0' and '1', '1' for inputs '2' and '3'. **d** Measured output of Device B (Bit 2): Output '0' for inputs '0' and '2', '1' for inputs '1' and '3'

and output '1' (amplitude > V_{TH}) for inputs '2' and '3'. Device B (bit 2) should output '0' (amplitude < V_{TH}) for inputs '0' and '2', and output '1' (amplitude > V_{TH}) for inputs '1' and '3'. We identify suitable operating frequency ranges that satisfy these conditions: ~ 40.05 MHz to ~ 41.3 MHz for device A, and ~33.7 MHz to ~ 34.2 MHz for device B (Fig. 5c, d), and these ranges offer operational flexibility. Referenced to the resonance frequency of f_0 at $V_{GS} = 0$ V, the operating band for device A corresponds to $f_0 + 2.55$ MHz to $f_0 + 3.77$ MHz, and for device B the range is $f_0 + 2.07$ MHz to $f_0 + 2.48$ MHz. We subsequently verify the basic logic performance by measuring the response amplitudes at fixed operating frequencies: 40.4 MHz for device A, and 34.0 MHz for device B, while cycling through inputs. The measurement results are consistent with the expected design and truth table, confirming the correct logic of the independently-tuned resonator array. This frequency-based approach suggests that the design can be applicable to other NEMS resonators with different materials or resonant frequencies.

The proposed decimal-to-binary converter building block fully leverages the strong frequency tunability of 2D NEMS resonators, and the signal amplification provided by their high Q factors, enabling low operating voltages and high SNRs for robust state discrimination. In comparison, for CMOS circuits, the design includes the logic-circuit encoder which consists of at least 12 MOSFETs, making it significantly more complex than our 2-resonantor solution (Supplementary Note S12). This approach also shows promise for implementing more complex systems such as analog-to-digital converters (ADCs), and other NEMS-based circuitry with reduced device count and complexity. In the future, to achieve synchronized logic operations and computing using multiple 2D NEMS resonators, unifying the operating frequency of the components, building the system with multiple lasers with simultaneous measurement, replacing laser readout by electrical method, and developing peripheral circuits are important and require further exploration.

Conclusion

We demonstrate a mass transfer printing method for fabricating 2D NEMS resonator arrays, yielding large-scale arrays of electronically-independent and individually-accessible monolayer and few-layer MoS_2 NEMS resonators, with physical separation between devices. Devices fabricated *via* the MTP method exhibit not only excellent crystal properties and well-defined suspended structures, but also resonant frequencies in the VHF range, *Q* factors comparable to other NEMS devices, considerable *SNR*s, and relatively uniform gate voltage tuning characteristics. Crucially, experiments confirm excellent electronic isolation between devices, enabling independent control of each resonator through individually-applied AC excitation or DC gate voltage. Leveraging such independence, a functional decimal-to-binary converter building block based on two adjacent 2D NEMS resonators is successfully demonstrated. The MTP fabrication technique paves the way towards scalable production of high-performance 2D NEMS resonator arrays, and plays a significant role in advancing the application of more complex NEMS systems requiring independent control and coordinated operation among multiple devices.

Acknowledgements
The authors thank the support from National Natural Science Foundation of China (NSFC) (Grants U21A20505, 92364107, U25A20496, W2512033), Science and Technology Commission of Shanghai Municipality (STCSM) (Grants 23QA1405300, 24ZR1491500), and the State Key Laboratory of Radio Frequency Heterogeneous Integration (Shenzhen University) Independent Scientific Research Program.

Author details
[1]Global College, Shanghai Jiao Tong University, Shanghai, China. [2]Frontier Institute of Chip and System, Fudan University, Shanghai, China. [3]State Key Laboratory of Radio Frequency Heterogeneous Integration, Shanghai Jiao Tong University, Shanghai, China

Data availability
All data needed to evaluate the conclusions in the paper are present in the paper and/or the Supplementary Information. All other relevant data of this study are available from the corresponding author upon reasonable request.

Competing interests
The authors declare no competing interests.

Supplementary information The online version contains supplementary material available at https://doi.org/10.1038/s41378-025-01132-w.

Received: 30 July 2025 Revised: 7 October 2025 Accepted: 3 November 2025
Published online: 08 January 2026

References
1. Lin, Y. et al. Recent advances in 2D material theory, synthesis, properties, and applications. *ACS Nano* **17**, 9694–97747 (2023).
2. Manzeli, S., Ovchinnikov, D., Pasquier, D., Yazyev, O. V. & Kis, A. 2D transition metal dichalcogenides. *Nat. Rev. Mater.* **2**, 17033 (2017).
3. Liu, Z. et al. Wafer-scale synthesis of two-dimensional materials for integrated electronics. *Chip* **3**, 100080 (2024).
4. Jung, M. et al. GHz nanomechanical resonator in an ultraclean suspended graphene p–n junction. *Nanoscale* **11**, 4355–4361 (2019).
5. Ye, F., Islam, A., Zhang, T. & Feng, P. X.-L. Ultrawide frequency tuning of atomic layer van der Waals heterostructure electromechanical resonators. *Nano Lett.* **21**, 5508–5515 (2021).
6. Lee, J. et al. Electrically tunable single- and few-layer MoS_2 nanoelectromechanical systems with broad dynamic range. *Sci. Adv.* **4**, eaao6653 (2018).
7. Zhang, P., Jia, Y., Liu, Z. & Yang, R. Strain-enhanced dynamic ranges in two dimensional MoS_2 and $MoTe_2$ nanomechanical resonators. *Appl. Phys. Rev.* **11**, 011410 (2024).
8. Xin, C. et al. Machine learning-accelerated discovery of novel 2D ferromagnetic materials with strong magnetization. *Chip* **2**, 100071 (2023).
9. Zhang, P., Jia, Y., Yuan, S., Liu, Z. & Yang, R. Tunable stochastic state switching in 2D MoS_2 nanomechanical resonators with nonlinear mode coupling and internal resonance. *Nano Lett.* **24**, 11043–11050 (2024).
10. Zhu, J. et al. Broad-range, high-linearity, and fast-response pressure sensing enabled by nanomechanical resonators based on 2D non-layered material: β-In_2S_3. *Infomat.* **6**, e12553 (2024).
11. Weber, P., Güttinger, J., Noury, A., Vergara-Cruz, J. & Bachtold, A. Force sensitivity of multilayer graphene optomechanical devices. *Nat. Commun.* **7**, 12496 (2016).
12. Dash, A., More, S. K., Arora, N. & Naik, A. K. Ultra-sensitive charge detection and latch memory using MoS_2-nanoresonator based bifurcation amplifiers. *Appl. Phys. Lett.* **118**, 053105 (2021).
13. Chen, C. et al. Graphene mechanical oscillators with tunable frequency. *Nat. Nanotechnol.* **8**, 923—927 (2013).
14. Tang, J. et al. HF-VHF NEMS resonators enabled by 2D semiconductor $ReSe_2$. *Sci. China Inf. Sci.* **67**, 209401 (2024).
15. Wang, L., Zhang, P., Liu, Z., Wang, Z. & Yang, R. On-chip mechanical computing: status, challenges, and opportunities. *Chip* **2**, 100038 (2023).
16. Zhang, P. et al. Nanoelectromechanical memories based on nonlinear 2D MoS_2 resonators. In *Proc. 35th IEEE Int. Conf. on Micro Electro Mechanical Systems (MEMS)*, 208–211 (IEEE, 2022).
17. Samanta, C. et al. Nonlinear nanomechanical resonators approaching the quantum ground state. *Nat. Phys.* **19**, 1340–1344 (2023).
18. Xu, B. et al. Nanomechanical resonators: toward atomic scale. *ACS Nano* **16**, 15545–15585 (2022).
19. Zhang, P. et al. Unveiling the tradeoff between device scale and surface nonidealities for an optimized quality factor at room temperature in 2D MoS_2 nanomechanical resonators. *Microsyst. Nanoeng.* **10**, 140 (2024).
20. Jia, H. et al. Single- and few-layer transfer-printed CVD MoS_2 nanomechanical resonators with enhancement by thermal annealing. In *Proc. IEEE International Frequency Control Symposium (IFCS)* 1–3 (IEEE, 2016).
21. Zheng, X., Gong, S., Geng, H. & Guo, Y. Mechanical energy dissipation pathways in Ga_2O_3 nanoelectromechanical resonators. *Acta Phys. Sin.* **74**, 078501 (2025).
22. Lee, J., Wang, Z., He, K., Shan, J. & Feng, P. X.-L. Air damping of atomically thin MoS_2 nanomechanical resonators. *Appl. Phys. Lett.* **105**, 023104 (2014).
23. Morell, N. et al. A high quality factor mechanical resonators based on WSe_2 monolayers. *Nano Lett.* **16**, 5102–5108 (2016).
24. van der Zande, A. M. et al. Large-scale arrays of single-layer graphene resonators. *Nano Lett.* **10**, 4869–4873 (2010).
25. Jia, H. et al. Large-scale arrays of single- and few layer MoS_2 nanomechanical resonators. *Nanoscale* **8**, 10677–10685 (2016).
26. Arjmandi-Tash, H., Allain, A., Han, Z. & Bouchiat, V. Large scale integration of CVD-graphene based NEMS with narrow distribution of resonance parameters. *2D Mater.* **4**, 025023 (2017).
27. Liu, Z. et al. Large-scale arrays of tunable monolayer MoS_2 nanoelectromechanical resonators. In *Proc. 36th IEEE Int. Conf. on Micro Electro Mechanical Systems (MEMS)*, 281–284 (IEEE, 2023).
28. Barton, R. A. et al. High, size dependent quality factor in an array of graphene mechanical resonators. *Nano Lett.* **11**, 1232–1236 (2011).
29. Liu, Z. et al. Polymethyl methacrylate pyrolysis assisted transfer of 2D materials for large-scale molybdenum disulfide NEMS resonator arrays. In *Proc. 37th IEEE Int. Conf. on Micro Electro Mechanical Systems (MEMS)*, 677–680 (IEEE, 2024).

30. Liu, L. et al. A mass transfer technology for high-density two-dimensional device integration. *Nat. Electron.* **8**, 135–146 (2025).
31. Carlson, A. et al. Transfer printing technology for materials assembly and micro/ nano device fabrication. *Adv. Mater.* **24**, 5284–5318 (2012).
32. Shen, Y.-C. et al. Rational design on wrinkle-less transfer of transition metal dichalcogenide monolayer by adjustable wettability-assisted transfer method. *Adv. Func. Mater.* **31**, 2104978 (2021).
33. Yang, R., Zheng, X., Wang, Z., Miller, C. J. & Feng, P. X.-L. Multilayer MoS_2 transistors enabled by a facile dry-transfer technique and thermal annealing. *J. Vac. Sci. Technol. B* **32**, 061203 (2014).
34. Xu, B. et al. Dynamic tuning of terahertz atomic lattice vibration via cross-scale mode coupling to nanomechanical resonance in WSe_2 membranes. *Microsyst. Nanoeng.* **11**, 18 (2025).
35. Li, S. et al. Functional PDMS elastomers: bulk composites, surface engineering, and precision fabrication. *Adv. Sci.* **10**, 2304506 (2023).
36. Yang, R. et al. Tuning optical signatures of single- and few-layer MoS_2 by blown-bubble bulge straining up to fracture. *Nano Lett.* **17**, 4568–4575 (2017).
37. Jeon, J. et al. Layer-controlled CVD growth of large-area two-dimensional MoS_2 films. *Nanoscale* **7**, 1688–1695 (2015).
38. Huang, Y. et al. An efficient route to prepare suspended monolayer for feasible optical and electronic characterizations of two-dimensional materials. *InfoMat.* **4**, e12274 (2022).
39. Costa, R. G., Barbosa, A. D. N., Maia da costa, M. E. H. & Freire, F. L. Resonance Raman spectroscopy of MoS_2 monolayers treated with nitrogen plasma. *Vib. Spectrosc.* **123**, 103454 (2022).
40. Lin, T.-Y. et al. Air gap-based cavities dramatically enhance the true intrinsic spectral signals of suspended and pristine two-dimensional materials. *J. Phys. Chem. C* **123**, 5667–5679 (2019).
41. Lee, J.-U., Kim, K. & Cheong, H. Resonant Raman and photoluminescence spectra of suspended molybdenum disulfide. *2D Mater.* **2**, 044003 (2015).
42. Lee, J., Wang, Z., He, K., Shan, J. & Feng, P. X.-L. High frequency MoS_2 nanomechanical resonators. *ACS Nano* **7**, 6086–6091 (2013).
43. Yang, R. et al. Raman spectroscopic probe for nonlinear MoS_2 nanoelectromechanical resonators. *Nano Lett.* **22**, 5780–5787 (2022).
44. Davidovikj, D. et al. Visualizing the motion of graphene nanodrums. *Nano Lett.* **16**, 2768–2773 (2016).
45. Kramer, E., van Dorp, J., van Leeuwen, R. & Venstra, W. J. Strain-dependent damping in nanomechanical resonators from thin MoS_2 crystals. *Appl. Phys. Lett.* **107**, 091903 (2015).
46. Zhang, P. et al. Strain-modulated dissipation in two-dimensional molybdenum disulfide nanoelectromechanical resonators. *ACS Nano* **16**, 2261–2270 (2022).
47. Miller, D., Blaikie, A. & Alemán, B. J. Nonvolatile rewritable frequency tuning of a nanoelectromechanical resonator using photoinduced doping. *Nano Lett.* **20**, 2378–2386 (2020).
48. Zhu, J., Zhang, P., Yang, R. & Wang, Z. Analyzing electrostatic modulation of signal transduction efficiency in MoS_2 nanoelectromechanical resonators with interferometric readout. *Sci. China Inf. Sci.* **65**, 122409 (2022).